Impact of Al$_2$O$_3$ Passivation on the Photovoltaic Performance of Vertical WSe$_2$ Schottky Junction Solar Cells

Elaine McVay,*,‡ Ahmad Zubair,‡ Yuxuan Lin, Amirhasan Nourbakhsh, and Tomás Palacios

Cite This: *ACS Appl. Mater. Interfaces* 2020, 12, 57987−57995

Read Online

ACCESS | Metrics & More | Article Recommendations | Supporting Information

ABSTRACT: Transition metal dichalcogenide (TMD) materials have emerged as promising candidates for thin-film solar cells due to their wide bandgap range across the visible wavelengths, high absorption coefficient, and ease of integration with both arbitrary substrates and conventional semiconductor technologies. However, reported TMD-based solar cells suffer from relatively low external quantum efficiencies (EQE) and low open circuit voltage due to unoptimized design and device fabrication. This paper studies Pt/WSe$_2$ vertical Schottky junction solar cells with various WSe$_2$ thicknesses in order to find the optimum absorber thickness. Also, we show that the devices' photovoltaic performance can be improved via Al$_2$O$_3$ passivation, which increases the EQE up to 29.5% at 410 nm wavelength incident light. The overall resulting short circuit current improves through antireflection coating, surface doping, and surface trap passivation effects. Thanks to the Al$_2$O$_3$ coating, this work demonstrates a device with an open circuit voltage (V_{OC}) of 380 mV and a short circuit current density (J_{SC}) of 10.7 mA/cm^2. Finally, the impact of Schottky barrier height inhomogeneity at the Pt/WSe$_2$ contact is investigated as a source of open circuit voltage lowering in these devices.

KEYWORDS: solar cell, WSe$_2$, passivation, energy harvesting, vertical Schottky diode, two-dimensional materials
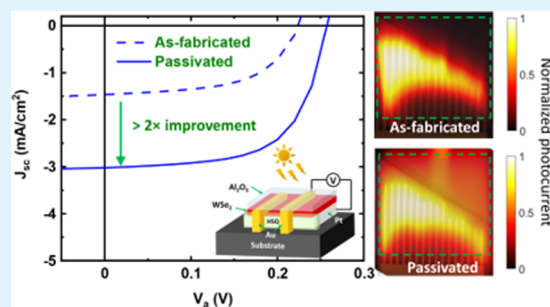
INTRODUCTION

Transition metal dichalcogenide (TMD) materials are emerging candidates for flexible thin-film photovoltaics to be used in applications such as internet of things, flexible electronics, and ubiquitous electronics[1] due to their high absorption coefficient,[2−4] mechanical flexibility,[5] high carrier mobility, and ultrathin nature.[6] Thanks to their weak van der Waals interlayer bonding, these materials (in their ideal form) offer a self-passivated surface free of dangling bonds that can also be heterogeneously integrated with bulk materials as tandem solar cells to maximize their photovoltaic efficiency.

Tungsten diselenide (WSe$_2$) is one of the most promising TMD materials due to its bulk bandgap of ∼1.3 eV[7] that offers maximum photovoltaic efficiency for a single absorber according to the Shockley−Queisser formalism.[8] The high electron and hole carrier mobility (greater than 100 cm^2/(V s))[9] and high absorption coefficient (i.e., 10^5 cm^{-1} at 780 nm[10] compared to silicon's 10^3 cm^{-1}) make it an attractive option for high-performance photovoltaic applications. Most of the earlier research efforts on TMD photovoltaics focus on the monolayer limit due the direct nature of the bandgap. However, monolayer TMDs can only absorb ∼10% of incident light,[6] and although this absorption could be increased with appropriate resonators, it is arguably more straightforward to simply use a thicker absorber layer. Recent works show that multilayer WSe$_2$ and other TMD materials can offer promising performance for thin-film photovoltaic applications. The ideal approach for TMD solar cell design is to use p-n junction diodes.[11,12] However, due to the lack of a reliable substitutional doping technology in TMD materials, research efforts have been mostly focused on Schottky junction solar cells. These devices offer a relatively simple fabrication process and the option to tune the open circuit voltage by work function engineering of the contact metal. Jariwala et al.[3] demonstrated that excellent (higher than 90%) absorption characteristics can be achieved for multilayer WSe$_2$ flakes (∼15 nm) by optimized photonic design (silver back reflector to maximize the absorption via Fabry−Perot effects). Recently, Went et al. demonstrated a novel metallization technique to improve the interface between the metal and the TMD absorber layer.[13] The authors show that transferred gold onto 16 nm WS$_2$ can form a large Schottky barrier leading to a PCE of 0.46% and an open circuit voltage of 0.256 V at AM1.5 illumination. Wi et al. studied several contact metals to WSe$_2$ and showed that the high Schottky barrier between Zn contacts and ∼100 nm-thick WSe$_2$ can increase the open circuit voltage (∼0.35 V)[14] but did not explore the effects of absorber layer thickness.
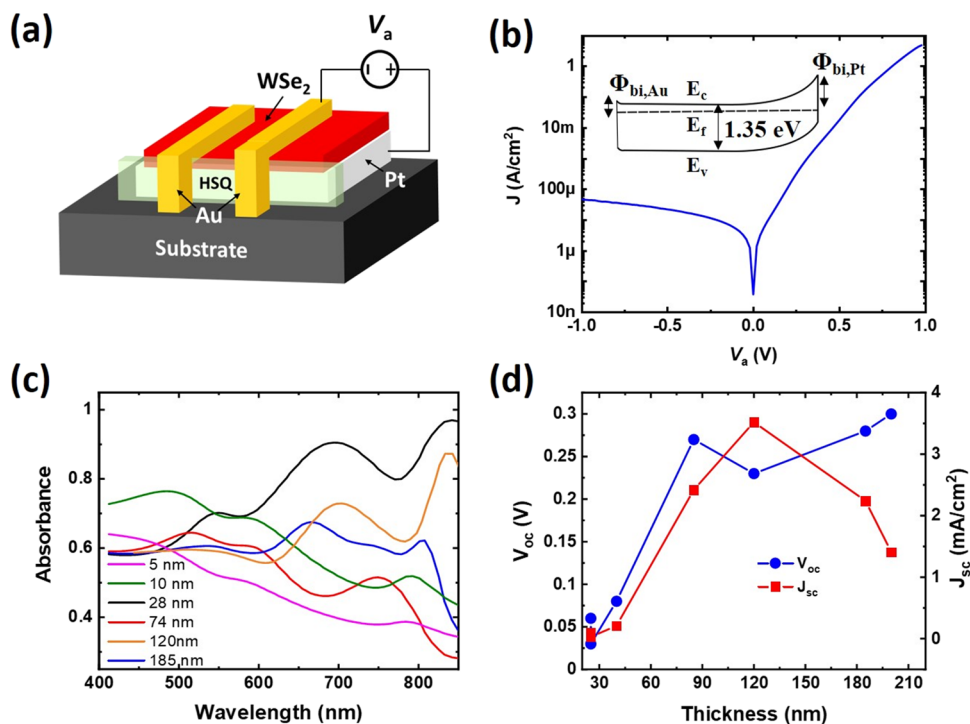
Figure 1. (a) Schematic diagram of the fabricated Schottky barrier solar cell, where a WSe_2 layer is sandwiched between top (Au) and bottom (Pt) metal contacts. An electron beam cross-linked HSQ layer is used as isolation dielectric between the two contacts. (b) Transport characteristics of a typical WSe_2 diode (device A, 185 nm) showing a rectification ratio > 10^4 at 1 V compared to −1 V. The inset shows the equilibrium (V_a = 0 V) energy band diagram under illumination. (c) Simulated absorption characteristics of layered WSe_2 on Pt back contact for different film thicknesses. (d) Open circuit voltage and short circuit current as a function of WSe_2 thickness (including devices A−D in the main text) under 0.3 W/m^2 broadband illumination.

Despite the excellent progress in optimizing the absorption and photonic design in WSe_2 Schottky junction solar cells, the demonstrated solar cell power conversion efficiency (0.8−6.7% measured at 532 nm illumination)[3,14] is still well below the expected theoretical values (20−27%).[2] To realize the ultimate potential of layered transition metal dichalcogenides in thin-film photovoltaics, it is necessary to also carefully design and understand the electronic transport, doping, and passivation technologies in these devices.[2,15,16]

This work demonstrates high work function platinum (Pt)/ WSe_2 vertical Schottky junction solar cell diodes using multilayer WSe_2 as the absorber layer. We explore the trade-off between absorber thickness and device performance as a function of observed V_{OC} and J_{SC} to identify the optimal thickness range (80−150 nm) for Schottky junction solar cell applications. We also study the impact of Al_2O_3 passivation on the fabricated WSe_2 solar cell performance. The passivated devices show dramatic improvement of the external quantum efficiency and short circuit current without impacting the open circuit voltage. Finally, we investigate the nonuniform distribution of Schottky barrier height across the Pt-to-WSe_2 contact, which lowers the effective Schottky barrier height, thus decreasing the open circuit voltage due to an increase in dark current. Although a further in-depth study is required to understand the effect of passivation and how to increase the uniformity of the Schottky contacts, our findings reveal a promising direction for improving the performance of the layered TMDC solar cells.

RESULTS AND DISCUSSION

A schematic of the device used in our study is shown in Figure 1a. The work function difference between the bottom electrode and the semiconductor absorber layer determines the open circuit voltage of the devices. The theoretical large work function difference (0.5 eV) between Pt and n-type WSe_2 (see Figure S1 for characterization of bulk doping) makes this metal an attractive option for the bottom electrode. Mechanically exfoliated and dry-transferred WSe_2 serves as the absorber layer with a patterned gold electrode on top for carrier collection. The gold electrodes form a nearly ohmic contact due to their negligible Schottky barrier height with WSe_2 (see Supporting Information Figure S2 for Au/WSe_2/Au $I−V$ characteristics).[17] A layer of electron beam-patterned hydrogen silsesquioxane (HSQ) serves as the isolation between top contact and sidewalls of WSe_2 to prevent in-plane conduction through WSe_2, which may contribute to the dark current. The device was then capped with an aluminum oxide (Al_2O_3) layer for passivation and charge transfer doping studies. Al_2O_3 is grown via a two-step deposition process by utilizing an electron beam-evaporated seed layer and a subsequent atomic layer deposition (ALD) layer. A list of specific devices discussed in the main text is summarized in Table 1, and detailed processing information is included in the Experimental Methods section.

Figure 1b shows the dark current−voltage characteristics of device A, a representative WSe_2 Schottky diode with $t_{WSe2} \approx$ 185 nm. The diode exhibits a well-defined rectifying behavior in the dark with a rectification ratio (current at 1 V of applied bias compared to −1 V applied bias) greater than 10^4. Under AM1.5 illumination, the device (after passivation with 12 nm

Table 1. Summary of Devices Discussed in the Main Text

device	thickness of the WSe$_2$ absorber layer (t_{WSe2})
A	185 nm
B	120 nm
C	74 nm
D	25 nm

Al$_2$O$_3$) shows photovoltaic performance with an open circuit voltage (V_{OC}) of 380 mV, a short circuit current density (J_{SC}) of 10.7 mA/cm^2, a fill factor of 44%, and a maximum generated power of 1.5 mW/cm^2 (see Supporting Information Figure S3, Figure S4, and Table S1). Figure 1c compares the simulated absorption of WSe$_2$ flakes of various thicknesses on Pt back contacts as calculated by the transfer matrix method[18] using n, k data extracted from the literature[19] (see details in Supporting Information section 5). It demonstrates a high broadband absorption, even down to the 10 nm-thick flake, of WSe$_2$ on Pt. However, the experimental results of fabricated devices shown in Figure 1d demonstrate better short circuit current performance in the devices with an absorber thickness in the 80−150 nm range. The relatively lower J_{SC} for absorber layers thinner than 120 nm can be attributed to a greater impact of the surface and metal/semiconductor interface recombination, impeding carrier separation for thinner flakes. In thicker devices, a greater percentage (particularly longer wavelength) of light is absorbed away from the interfaces. Carriers can then be generated in a region of the semiconductor that has a recombination time constant dominated by bulk effects and can be separated by the metal/semiconductor defined electric field. Similar J_{SC} lowering trends due to interfacial recombination were observed in published simulations that studied the thickness scaling of Si solar cells.[20] Meanwhile, the J_{SC} roll-off for flakes thicker than 120 nm can be explained by the fact that

for active regions with thicknesses greater than the depletion region, there is little to no band bending at the air/WSe$_2$ interface. If we set $\varphi_{bi} \approx \varphi_{bn} = 0.23$ eV, $\varepsilon_s = 8.7$,[21] and $N_d = 1.5 \times 10^{16} \frac{1}{cm^3}$ (extraction of these parameters appears later in the text and the Supporting Information), then we can apply the depletion approximation to estimate a depletion region of 148 nm. Coupled with a low vertical mobility of 0.01 cm^2/(V s) and a bulk recombination time constant of about 50 ns,[22] we can expect that carriers generated by light (particularly short wavelength) absorbed near the surface and outside of the device's depletion region are not efficiently collected at the contacts. In addition, more long wavelength light (∼690 nm and greater) is absorbed in the 120 nm WSe$_2$ layer on Pt than in the 185 nm WSe$_2$ layer on Pt (see Supporting Information Figure S6b). We have included a more detailed discussion on the J_{SC} and V_{OC} and a function of WSe$_2$ thickness in Supporting Information section 6 with reference to Supporting Information Figures S6 and S7. We use devices B and C that are within the optimal intermediate thickness range for detailed passivation studies.

In conventional and thin-film solar cells, passivation[15,16] can further improve device performance and stability. Passivation plays an important role in semiconductor devices by protecting the surface, removing defects, and managing the electric field profile, as well as acting as an antireflection coating. Recent works have shown that Al$_2$O$_3$ can be used to passivate and n-type dope MoS$_2$ transistors[17] and photodetectors.[23] Al$_2$O$_3$ was also used to improve the PCE of a MoS$_2$/Si solar cell, although the dominant mechanism for the improved passivation was not investigated.[24] In addition to these devices, a related work uses the hole transport layer WO$_x$ on WSe$_2$ to induce p-type doping in a heterojunction solar cell.[25] Here, we systematically study the impact of Al$_2$O$_3$ passivation on Schottky junction WSe$_2$
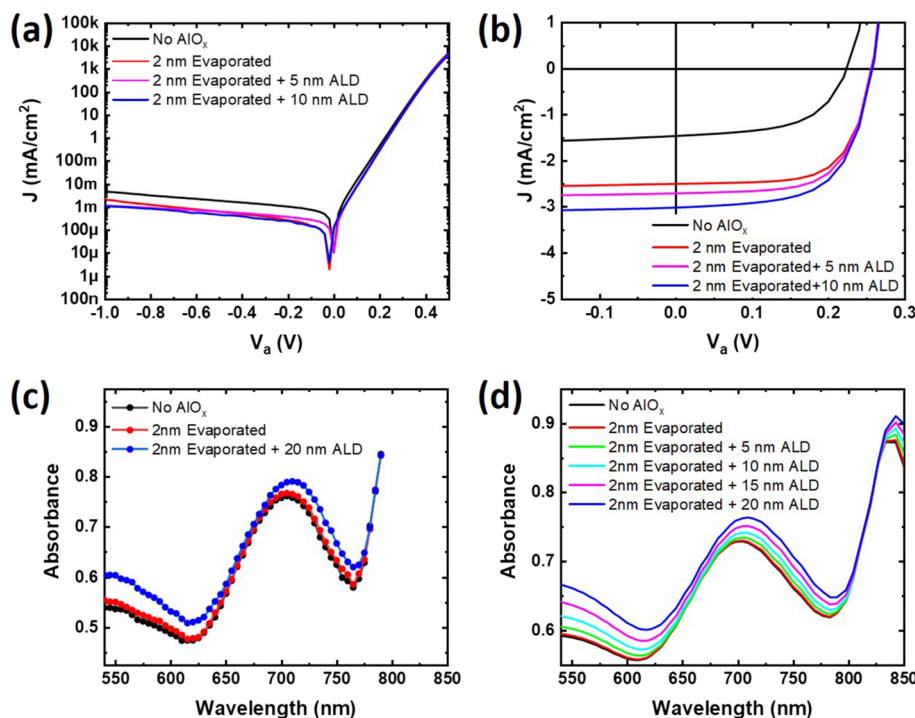

Figure 2. (a) Dark current characteristics of the pristine and Al$_2$O$_3$ passivated devices for various thicknesses of Al$_2$O$_3$ deposited onto the 120 nm-thick WSe$_2$ layer of device B. (b) Photovoltaic characteristics of the pristine and passivated device measured under a 30 mW/cm^2 3400 K black body source. (c) Absorbance of the pristine and passivated device. (d) Simulated absorbance of the pristine and passivated device.
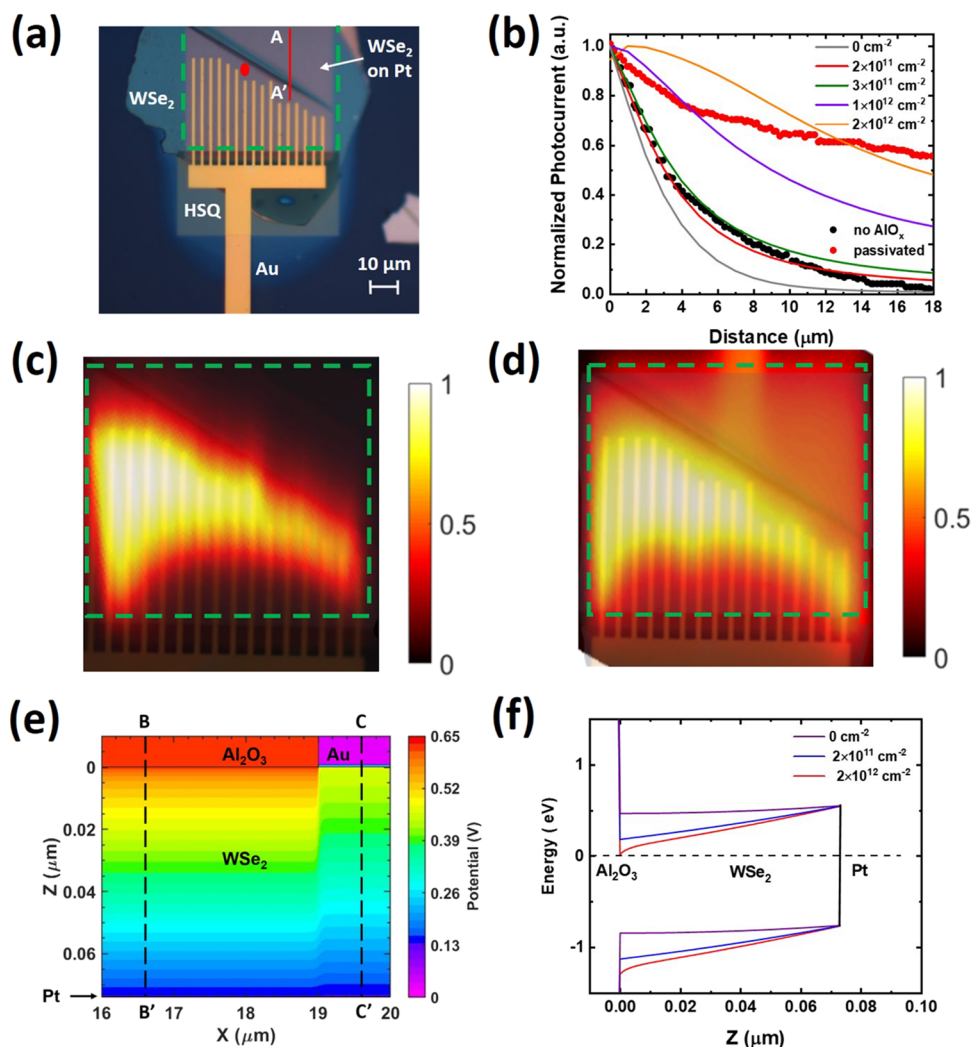
Figure 3. (a) Optical image of device C depicting point of measurement for the EQE and power dependence (red dot). The green dashed line outlines the active device area. The top electrode has a trapezoidal shape to avoid a wrinkle in the flake. (b) Normalized photocurrent (symbols) profile along A′A of the device in the pristine state and with Al_2O_3 passivation compared to simulated device characteristics (solid lines). (c,d) Photocurrent map of the pristine and passivated device, with a 1 μm spot size laser beam at 532 nm and 12 μW. The green dashed line shows the bottom platinum (Pt) contact. (e) Simulated potential profile of the passivated device with 10^{12} cm^{-2} surface charge. (f) Energy band diagram across BB′ showing comparison between simulated devices as a function of positive surface charge density.

solar cell performance. We identify and quantify three mechanisms through which Al_2O_3 passivation improves device performance: surface trap passivation, surface doping, and antireflection coating effects.

The effect of the Al_2O_3 passivation layer thickness on the solar cell performance was investigated in detail on device B with the optimum WSe$_2$ thickness ($t_{WSe2} = 120$ nm). Figure 2a shows the change in the dark current due to Al_2O_3. The high forward bias region shows little change after passivation (series resistance is unchanged), and the ideality factor remains at ~1.28 (see Supporting Information Table S2) for all passivation thicknesses, suggesting that bulk recombination processes are unchanged in the diode. However, the low forward bias (highlighted in Figure S8a) and reverse bias regions (highlighted in Figure S8b) show suppression of dark current upon passivation. Figure 2b shows the change in photovoltaic characteristics as a function of the Al_2O_3 passivation layer thickness. The initial 2 nm electron beam-evaporated Al_2O_3 shows the largest relative improvement (69%) in J_{SC} from 18.3 to 31 nA. The further addition of Al_2O_3

passivation shows relatively smaller improvement in J_{SC}. An additional 5 nm ALD Al_2O_3 shows 8.3% increment in J_{SC}, while the relative improvement is slightly larger (11.3%) for another 10 nm of ALD Al_2O_3 compared with the 5 nm ALD Al_2O_3. This suppression of the reverse bias dark current along with the increase in short circuit current can explain the improvement in the open circuit voltage seen in Figure 2b from 0.22 to 0.25 V. Further, the largest relative improvement due to passivation is seen between the unpassivated case and the 2 nm AlO$_x$ cases, and additional AlO$_x$ thickness provides incremental improvement to the short circuit current.

From the results of Figure 2b, the short circuit current could be improved due to any combination of passivation of trap states, doping of tungsten diselenide, and antireflection coating effects of Al_2O_3. To identify the origin of short circuit current improvement, the absorbance characteristics of the WSe$_2$ flake are measured under a broadband white light source before passivation and compared with 2 nm electron beam-evaporated Al_2O_3 and additional 20 nm ALD passivation. As shown in Figure 2c and Supporting Information Figure S9a,

the change in the absorbance due to the 2 nm passivation is negligible (~1%), while the improvement due to the additional 20 nm ALD passivation reaches a value of 12% at the 550 nm wavelength. The simulated absorbance in Figure 2d and Supporting Information Figure S9b for different passivation thicknesses confirms the experimental observations. The marginal improvement in the absorption due to 2 nm AlO_x compared to the 69.4% increase in the short circuit current indicates that the antireflection coating effect of Al_2O_3 cannot alone explain the large increase in short circuit current. Instead, we conclude from this experiment that the 2 nm AlO_x coating improves the device performance through a combination of surface doping and surface trap passivation.

To further understand the effect of Al_2O_3 on the short circuit current improvement, we map photocurrent under short circuit conditions ($V_a = 0$ V) and measure the external quantum efficiency (EQE) at the 532 nm wavelength for device C ($t_{WSe2} = 74$ nm). Figure 3a shows the top-view optical image of the device. A cross section of the normalized photocurrent (symbols) along the A′-A line depicted in Figure 3b shows relatively higher and more uniform photocurrent collection away from the top electrodes (ohmic contacts) in the passivated device. To study the effect of surface doping, the device was modeled using Silvaco Atlas (see Supporting Information section 9 and Table S5 for details). Interestingly, the simulated curve for 2×10^{11} cm^{-2} surface doping shows a good match with our experimental results (black symbols), suggesting that unpassivated devices may have some fixed positive charge at the surface that causes electrons in WSe_2 to accumulate near the surface to maintain charge neutrality at the interface. These positive fixed charges are likely due to selenium vacancies[26,27] induced on the surface during our 350 °C annealing step during fabrication. The simulated curves also show that increases in positive surface charge lead to large improvements in photocurrent collection away from the top electrode. The improvement in photocurrent monotonically increases with the positive surface charge density. The simulation further indicates that the passivated case can be qualitatively matched with ~2×10^{12} cm^{-2} surface doping, suggesting that AlO_x indeed adds charge to dope the surface of WSe_2. This value is in agreement with the literature, which suggests that AlO_x can be used to dope surfaces with up to 4×10^{12} cm^{-2} positive charge.[28] Likewise, the normalized photocurrent maps for pristine and passivated devices presented in Figure 3c and d, respectively, show an enlargement of the effective device active area for photocurrent generation after the Al_2O_3 passivation. As the electric field across an absorber layer is increased, the collected photocurrent as a function of lateral position becomes more uniform, and the decay profile broadens due to an increase in the drift length $L_E = \mu E \tau$, where τ, μ, and E are the lifetime, mobility, and the electric field.[29,30] Figure S11 shows that the electric field increases monotonically through the flake along the BB′ line, with a 24% increase in the electric field at 40 nm from the surface when comparing the 2×10^{11} and 2×10^{12} cm^{-2} doping cases. The resultant increase in L_E allows for more efficient minority carrier separation. Figure 3e shows the cross-sectional potential profile of the passivated device simulated using Silvaco Atlas to further study the impact of the surface doping on the electrostatics. The positive surface doping induced by Al_2O_3 contributes additional n-type band bending (and electric field) near the surface of the device, as shown in Figure 3f. The electric field engineering near the surface of the device due to the n-type

charge transfer doping increases the area available for photocurrent extraction for this device geometry. Interestingly, Supporting Information Figure S11 shows that for input powers of 0.1 $\mu W/\mu m^2$ and lower, the 1×10^{12} cm^{-2} positive surface charge doping can be used to yield 95% or greater normalized photocurrent across the WSe_2 absorber over a distance of 18 μm away from the Au electrode. The results of Figure 3 and Supporting Information Figure S12 suggest that the Al_2O_3 passivation could allow for more widely spaced gold electrodes in an optimized design.

Figure 4a and b demonstrates the wavelength dependence of the device's absorption and EQE with and without passivation. Both absorption and EQE measurements show peaks in the data near 760 nm due to the A-exciton[31] in bulk WSe_2. The B-exciton is located between 550 and 600 nm,[32] which likewise contributes to the increase seen in the EQE and absorption characteristics[10] in this wavelength range. We note that the
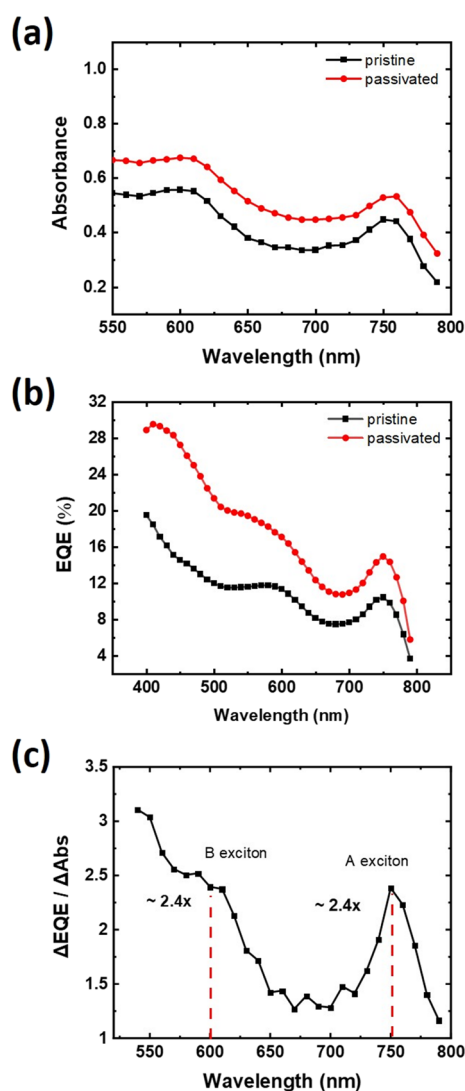
Figure 4. (a) Absorption of the pristine and of the 20 nm ALD passivated device C (74 nm flake) as a function of wavelength. (b) EQE of the pristine and passivated device as a function of wavelength. Measurements were taken using a 1 μm beam spot size with approximately 20 μW power at the same location. (c) Comparison of the change in EQE to the change in absorption to highlight regions where the change in EQE is far greater than the change in absorption.
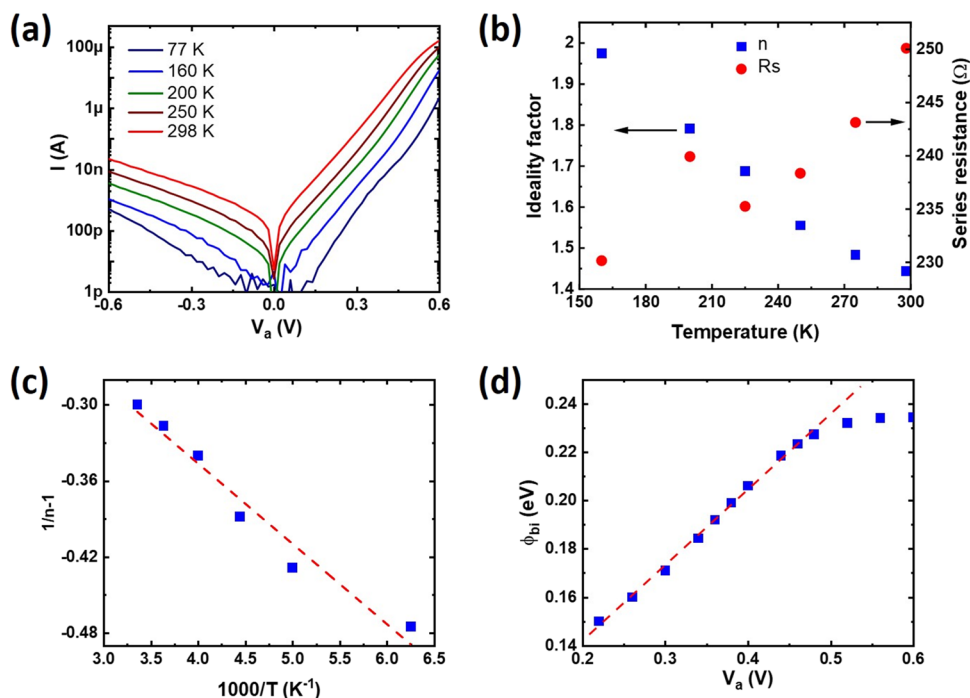
Figure 5. (a) Logarithmic plot of the device dark current vs applied bias for pristine device D with a 25 nm WSe$_2$ flake. (b) Ideality factor and series resistance as a function of temperature. (c) Ideality factor analysis according to Werner's methods. (d) Extracted Schottky barrier heights as a function of the applied bias voltage.

broadband improvement in the absorption in device C is not the same as the improvement in the absorption in device B due to different Fabry−Perot interference patterns (which are a function of the reflection coefficients at each interface, the complex index of refraction of each material, and the thickness of each layer in the stack as shown in equation S1) for material stacks with different thicknesses. However, the absorption improvement is again consistent with simulation as shown in Supporting Information Figure S13. Because both devices were fabricated according to the same process and use WSe$_2$ flakes extracted from the same crystal, we expect the surface doping and surface trap passivation effects to remain the same. Figure 4c shows the relative change in the EQE compared to the relative change in the absorption. Here, it can be seen that between the 650 and 700 nm wavelengths, the EQE improvement is mostly due to Al$_2$O$_3$'s antireflection coating effect. At higher wavelengths and near the 760 nm A-exciton peak, we observe large enhancement in the EQE that is not attributed simply to absorption improvement. From the discussion on Figure 3, we can point to surface doping as one mechanism to improve the EQE. However, Figure S14 also shows through simulation that the photocurrent magnitude near the Au cathode will increase if the surface recombination (srv) is decreased. Therefore, we suggest that this wavelength-dependent enlargement of the EQE is due to the surface doping identified by the photocurrent spatial mapping as well as the passivation of traps that reduce the surface recombination.

Both the passivated and pristine EQE results shown in Figure 4b highlight the need to improve the EQE at longer wavelengths to achieve high efficiency devices. The EQE reaches a maximum of 29.5% at 410 nm but is below 20% at 750 nm, which still is a wavelength above the indirect bandgap of ∼1.31 eV (947 nm). We additionally observed an EQE of 38.4% at 410 nm and 19.7% at 750 nm at a different

measurement location from the one tracked in Figure 4 (see Supporting Information Figure S15). A tandem solar cell with a material that more efficiently absorbs at the longer wavelengths or incorporates plasmonic structures, up-converting materials, or passivation layers that improve the device performance in this long wavelength region can potentially overcome this limitation.

In an ideal Schottky junction solar cell, the maximum expected open circuit voltage is approximately equal to the Schottky barrier height between the metal and the semiconductor. Although this work reports a high Schottky diode V_{OC} value at AM1.5 illumination (up to 0.38 V), this experimentally observed value is small considering platinum's work function of ∼6.0 eV[33] and WSe$_2$'s electron affinity of ∼4.0 eV.[7] To investigate the origin of the discrepancy between expected and experimentally observed V_{OC}, we perform systematic temperature-dependent transport measurement of the WSe$_2$ Schottky diode. Due to the van der Waals nature of the interlayer bonding, the vertical series resistance of the 185 nm-thick WSe$_2$ diode is expected to be very high, and it may lead to inaccurate extraction of the Schottky diode parameters. To overcome this limitation, we fabricated a device on a thinner WSe$_2$ layer, device D (t_{WSe2} = 25 nm). The analysis was repeated in Supporting Information Figure S16 for a device based on a 150 nm flake (device E), which shows a similar trend, but the result is affected by the large R_S. Neither device D nor device E was passivated as we do not expect that Al$_2$O$_3$ passivation on the top surface will affect the Pt/WSe$_2$/Au junction.

Figure 5a shows the temperature-dependent transport characteristics of device D. Temperature dependence of the reverse bias characteristics suggests the existence of trap-assisted tunneling processes[34] because a low effective Schottky barrier height (see Supporting Information Figure S17) was extracted at V_a = −0.42 V, and in this bias region, the Fowler−

Nordheim plot (see Supporting Information Figure S18) of the $I-V$ characteristics is temperature-dependent and the $\log\left(\frac{I}{V^2}\right)$ vs $\frac{1}{V}$ relationship is nonlinear. Meanwhile, the temperature dependence of the forward bias region indicates thermionic emission dominated current. From the Arrhenius plot,[35] a maximum Schottky barrier height of 0.23 eV is extracted for Pt/WSe$_2$. This barrier height is lower compared to the previously demonstrated experimental values and suggests the existence of Fermi pinning as well as barrier height inhomogeneities.[36] The low barrier height limits our maximum obtainable V_{OC} and has also been observed in transferred Au/WSe$_2$ contacts.[13] Contrary to the Pt/WSe$_2$ case, the ebeam lithography defined Au/WSe$_2$ contact is not dominated by thermionic emission as can be seen from its weak temperature dependence (see Supporting Information Table S7), allowing us to apply the single Schottky junction model in our analysis.

Schottky barrier inhomogeneity is a common phenomenon in bulk semiconductor devices[36,37] but is typically ignored in the analysis of layered material devices. The barrier between a metal and a semiconductor can be inhomogeneous due to the fabrication process or polycrystalline nature of the semiconductor. Ignoring Schottky barrier inhomogeneity may lead to inaccurate extraction of the barrier height. The level of inhomogeneity can be extracted from the ideality factor at low and high biases by using the methodology of Werner and Güttler.[36]

The ideality factor was extracted from both the low bias region, (via dI/dV) and the high bias region (see Supporting Information Table S7) (via a Norde plot), demonstrating that the ideality factor decreases with temperature and has a value of 1.45 at room temperature as shown in Figure 5b. The ideality factor of a Schottky diode with an inhomogeneous Schottky barrier can be expressed as

$$\frac{1}{n(T)} - 1 = \frac{\rho_2}{\frac{2k_bT}{q}} - \rho_1 \tag{1}$$

where $n(T)$ is the temperature-dependent ideality factor, ρ_1 is the difference between the mean barrier height at zero bias and the mean barrier height at applied bias V_a, and ρ_2 is the difference between the standard deviation at zero bias and the standard deviation at applied bias V_a. Figure 5c shows that $\frac{1}{n(T)} - 1$ is always positive, similar to PtSi/Si Schottky diodes,[36] indicating that the effective barrier height increases with increasing bias. We extract the values of ρ_1 and ρ_2 coefficients to be .0896 and −0.0111, respectively, from fitting a straight line to the data presented in Figure 5c. The negative value of ρ_2 indicates that barrier height distribution homogenizes with increasing bias. In comparison to Werner's PtSi/Si Schottky diodes, our Pt/WSe$_2$ diodes show a 2× higher ρ_2 coefficient, suggesting that this diode's barrier height distribution is strongly affected by the applied bias. This observation indicates that the Schottky barrier height inhomogeneities lower the effective barrier height within the regime of solar cell operation, thus lowering the open circuit voltage from its potentially higher value.

Figure 5d shows that the barrier height increases monotonically with the applied bias even after the barrier height estimation is corrected for inhomogeneities. A secondary conduction mechanism, i.e., a parallel leakage path,[38] causes the effective Schottky barrier height to decrease with decreasing voltage. At high bias, the thermionic emission current dominates, increasing the Schottky barrier height until it eventually saturates (Figure 5d). This leakage path contributes to additional open circuit voltage lowering.

■ CONCLUSION

In this work, we demonstrate high work function Pt/WSe$_2$ vertical Schottky junction solar cell diodes using multilayer WSe$_2$ as the absorber layer. We identify the 80−150 nm WSe$_2$ thickness range as optimal for photovoltaic performance, investigate the effect of Al$_2$O$_3$ passivation on device performance, and evaluate the nature of Schottky barrier height inhomogeneities that reduce the effective barrier height and solar cell V_{OC}. The effects of Al$_2$O$_3$ passivation on solar cell characteristics show clear short circuit improvement due to an improved EQE and photocurrent collection area. The improvement in EQE can be attributed to passivation of trap states, antireflection coating effects, and an altered carrier collection pathway due to doping. We show >50% higher EQE at wavelengths below 600 nm. More broadly, surface passivation techniques such as the one presented here can be used as a facile way to tune the performance of a TMD optoelectronic device for a desired application.

■ EXPERIMENTAL METHODS

Schottky diodes were fabricated on silicon wafers with 90 nm SiO$_2$ thermal oxide on top for convenient flake identification. Titanium (5 nm)/platinum (45 nm) electrodes were patterned via electron beam lithography and electron beam deposition. The surface of the Pt layer was cleaned with Nanostrip, 50:1 HF/H$_2$O, and ozone for 2 min prior to flake transfer. WSe$_2$ flakes were extracted from a bulk crystal from HQ Graphene by micromechanical exfoliation and subsequently transferred on top of the prepatterned electrodes using a pickup and dry transfer method.[39] After transfer, the flakes were cleaned in hot acetone followed by 350 °C annealing in a N$_2$ environment for 3.5 h to remove polymer residues from the dry transfer process. This step is necessary to ensure higher-quality top contact. Next, an isolation border was patterned onto the edge of the WSe$_2$ flake using electron beam exposed hydrogen silsesquioxane (HSQ) spin coated onto the sample to prevent conduction through the edge of the flake, which may have different properties than the bulk vertical conduction.[40,41] Then, ohmic contacts were patterned onto the WSe$_2$ flakes using electron beam lithography. Gold contacts were deposited in low pressure (<5 × 10^{-7} Torr) to reduce the contact resistance of the device.[17] Finally, Al$_2$O$_3$ coatings were applied to all devices except device D. The first 2 nm of passivation is deposited as aluminum via electron beam evaporation to act as a seeding layer for subsequent ALD layers to promote growth uniformity. The electrical characterization was performed using a B1500 semiconductor parameter analyzer. The low-temperature measurements were conducted in a Lakeshore cryogenic probe station using liquid nitrogen as a coolant. Solar simulator measurements were conducted at an AM1.5 workstation with a calibrated lamp.

For the scanning photocurrent measurements, a broadband supercontinuum fiber laser (Fianium) was combined with a monochromator to generate the monochromic laser beam with the desired wavelength. A two-axis piezo-controlled scanning mirror was coupled to a microscope objective through two confocal lenses to perform the spatial scanning with the laser beam spot of around 1 μm on the device. The photocurrent and the reflected light intensity were recorded simultaneously to form the scanning photocurrent images and the reflectance images. The photocurrent results were measured under the short circuit condition, in which zero voltage bias was applied across the device. The absorbance and EQE measurements were carried out with the same setup. The incident laser power was measured at the output of the microscope objective using a calibrated photodetector, and the reflected laser power was measured with

another photodetector at a divided beam path location after a beam splitter that was inserted before the input of the objective. The reflectance was calculated by normalizing the measured reflected power spectrum on the devices by the measured reflected power spectrum on a silver mirror.

■ ASSOCIATED CONTENT

ⓢ Supporting Information

The Supporting Information is available free of charge at https://pubs.acs.org/doi/10.1021/acsami.0c15573.

Additional data concerning $C–V$ characteristics, transfer matrix method and Silvaco Atlas simulation details, detailed description of trends observed in Figure 1d, simulated band diagrams, simulated photocurrent, simulated absorbance of device C, additional EQE data, and detailed explanation of our low-temperature analysis (PDF)

■ AUTHOR INFORMATION

Corresponding Author

Elaine McVay − *Department of Electrical Engineering Computer Science, Massachusetts Institute of Technology, Cambridge, Massachusetts 02139, United States;* ⓘ orcid.org/0000-0002-6572-3432; Email: emcvay@mit.edu

Authors

Ahmad Zubair − *Department of Electrical Engineering Computer Science, Massachusetts Institute of Technology, Cambridge, Massachusetts 02139, United States;* ⓘ orcid.org/0000-0001-9827-3557

Yuxuan Lin − *Department of Electrical Engineering Computer Science, Massachusetts Institute of Technology, Cambridge, Massachusetts 02139, United States;* ⓘ orcid.org/0000-0003-0638-2620

Amirhasan Nourbakhsh − *Department of Electrical Engineering Computer Science, Massachusetts Institute of Technology, Cambridge, Massachusetts 02139, United States*

Tomás Palacios − *Department of Electrical Engineering Computer Science, Massachusetts Institute of Technology, Cambridge, Massachusetts 02139, United States;* ⓘ orcid.org/0000-0002-2190-563X

Complete contact information is available at:
https://pubs.acs.org/10.1021/acsami.0c15573

Author Contributions

‡E.M. and A.Z. contributed equally. The manuscript was written through contributions of all authors. All authors have given approval to the final version of the manuscript.

Notes

The authors declare no competing financial interest.

■ ACKNOWLEDGMENTS

■ REFERENCES

(1) Koman, V. B.; Liu, P.; Kozawa, D.; Liu, A. T.; Cottrill, A. L.; Son, Y.; Lebron, J. A.; Strano, M. S. Colloidal Nanoelectronic State Machines Based on 2D Materials for Aerosolizable Electronics. *Nat. Nanotechnol.* **2018**, *13*, 819−827.

(2) Jariwala, D.; Davoyan, A. R.; Wong, J.; Atwater, H. A. Van der Waals Materials for Atomically-Thin Photovoltaics: Promise and Outlook. *ACS Photonics* **2017**, *4*, 2962−2970.

(3) Jariwala, D.; Davoyan, A. R.; Tagliabue, G.; Sherrott, M. C.; Wong, J.; Atwater, H. A. Near-Unity Absorption in van der Waals Semiconductors for Ultrathin Optoelectronics. *Nano Lett.* **2016**, *16*, 5482−5487.

(4) Wong, J.; Jariwala, D.; Tagliabue, G.; Tat, K.; Davoyan, A. R.; Sherrott, M. C.; Atwater, H. A. High Photovoltaic Quantum Efficiency in Ultrathin van der Waals Heterostructures. *ACS Nano* **2017**, *11*, 7230−7240.

(5) Lin, P.; Zhu, L.; Li, D.; Xu, L.; Pan, C.; Wang, Z. Piezo-Phototronic Effect for Enhanced Flexible MoS_2/WSe_2 van der Waals Photodiodes. *Adv. Funct. Mater.* **2018**, 1802849.

(6) Furchi, M. M.; Pospischil, A.; Libisch, F.; Burgdörfer, J.; Mueller, T. Photovoltaic Effect in an Electrically Tunable van der Waals Heterojunction. *Nano Lett.* **2014**, *14*, 4785−4791.

(7) Kim, K.; Larentis, S.; Fallahazad, B.; Lee, K.; Xue, J.; Dillen, D. C.; Corbet, C. M.; Tutuc, E. Band Alignment in WSe_2-Graphene Heterostructures. *ACS Nano* **2015**, *9*, 4527−4532.

(8) Shockley, W.; Queisser, H. J. Detailed Balance Limit of Efficiency of p-n Junction Solar Cells. *J. Appl. Phys.* **1961**, *32*, 510−519.

(9) Schmidt, H.; Giustiniano, F.; Eda, G. Electronic Transport Properties of Transition Metal Dichalcogenide Field-Effect Devices: Surface and Interface Effects. *Chem. Soc. Rev.* **2015**, *44*, 7715−7736.

(10) Frindt, R. F. The Optical Properties of Single Crystals of $WSe2$ and $MoTe2$. *J. Phys. Chem. Solids* **1963**, *24*, 1107−1108.

(11) Choi, M. S.; Qu, D.; Lee, D.; Liu, X.; Watanabe, K.; Taniguchi, T.; Yoo, W. J. Lateral MoS_2 p-n Junction Formed by Chemical Doping for Use in High-Performance Optoelectronics. *ACS Nano* **2014**, *8*, 9332−9340.

(12) Tang, Y.; Wang, Z.; Wang, P.; Wu, F.; Wang, Y.; Chen, Y.; Wang, H.; Peng, M.; Shan, C.; Zhu, Z.; Qin, S.; Hu, W. WSe_2 Photovoltaic Device Based on Intramolecular p-n Junction. *Small* **2019**, *15*, 1805545.

(13) Went, C. M.; Wong, J.; Jahelka, P. R.; Kelzenberg, M.; Biswas, S.; Hunt, M. S.; Carbone, A.; Atwater, H. A. A New Metal Transfer Process for van der Waals Contacts to Vertical Schottky-Junction Transition Metal Dichalcogenide Photovoltaics. *Sci. Adv.* **2019**, *5*, eaax6061.

(14) Wi, S.; Chen, M.; Li, D.; Nam, H.; Meyhofer, E.; Liang, X. Photovoltaic Response in Pristine WSe_2 Layers Modulated by Metal-Induced Surface-Charge-Transfer Doping. *Appl. Phys. Lett.* **2015**, *107*, No. 062102.

(15) Saint-Cast, P.; Benick, J.; Kania, D.; Weiss, L.; Hofmann, M.; Rentsch, J.; Preu, R.; Glunz, S. W. High-Efficiency c-Si Solar Cells Passivated With ALD and PECVD Aluminum Oxide. *IEEE Electron Device Lett.* **2010**, *31*, 695−697.

(16) Dingemans, G.; Seguin, R.; Engelhart, P.; Sanden, M. C. M. v. d.; Kessels, W. M. M. Silicon Surface Passivation by Ultrathin Al_2O_3 Films Synthesized by Thermal and Plasma Atomic Layer Deposition. *Phys. Status Solidi RRL* **2010**, *4*, 10−12.

(17) Yu, L.; Zubair, A.; Santos, E. J. G.; Zhang, X.; Lin, Y.; Zhang, Y.; Palacios, T. High-Performance WSe_2 Complementary Metal Oxide Semiconductor Technology and Integrated Circuits. *Nano Lett.* **2015**, *15*, 4928−4934.

(18) Pettersson, L. A. A.; Roman, L. S.; Inganäs, O. Modeling Photocurrent Action Spectra of Photovoltaic Devices Based on Organic Thin Films. *J. Appl. Phys.* **1999**, *86*, 487−496.

(19) Li, Y.; Chernikov, A.; Zhang, X.; Rigosi, A.; Hill, H. M.; van der Zande, A. M.; Chenet, D. A.; Shih, E.-M.; Hone, J.; Heinz, T. F. Measurement of the Optical Dielectric Function of Monolayer

Transition-Metal Dichalcogenides: MoS_2, $MoSe_2$, WS_2, and WSe_2. *Phys. Rev. B* **2014**, *90*, 205422.

(20) Islam, R.; Saraswat, K. Limitation of Optical Enhancement in Ultra-thin Solar Cells Imposed by Contact Selectivity. *Sci. Rep.* **2018**, *8*, 8863.

(21) Kumar, A.; Ahluwalia, P. K. Tunable Dielectric Response of Transition Metals Dichalcogenides MX2 (M=Mo, W; X=S, Se, Te): Effect of Quantum Confinement. *Phys. B* **2012**, *407*, 4627–4634.

(22) Massicotte, M.; Schmidt, P.; Vialla, F.; Schädler, K. G.; Reserbat-Plantey, A.; Watanabe, K.; Taniguchi, T.; Tielrooij, K. J.; Koppens, F. H. L. Picosecond Photoresponse in van der Waals Heterostructures. *Nat. Nanotechnol.* **2016**, *11*, 42–46.

(23) Kufer, D.; Konstantatos, G. Highly Sensitive, Encapsulated MoS_2 Photodetector with Gate Controllable Gain and Speed. *Nano Lett.* **2015**, *15*, 7307–7313.

(24) Rehman, A. U.; Khan, M. F.; Shehzad, M. A.; Hussain, S.; Bhopal, M. F.; Lee, S. H.; Eom, J.; Seo, Y.; Jung, J.; Lee, S. H. n-MoS_2/p-Si Solar Cells with Al_2O_3 Passivation for Enhanced Photogeneration. *ACS Appl. Mater. Interfaces* **2016**, *8*, 29383–29390.

(25) Yang, S.; Cha, J.; Kim, J. C.; Lee, D.; Huh, W.; Kim, Y.; Lee, S. W.; Park, H. G.; Jeong, H. Y.; Hong, S.; Lee, G. H.; Lee, C. H. Monolithic Interface Contact Engineering to Boost Optoelectronic Performances of 2D Semiconductor Photovoltaic Heterojunctions. *Nano Lett.* **2020**, *20*, 2443–2451.

(26) Tosun, M.; Chan, L.; Amani, M.; Roy, T.; Ahn, G. H.; Taheri, P.; Carraro, C.; Ager, J. W.; Maboudian, R.; Javey, A. Air-Stable n-Doping of WSe_2 by Anion Vacancy Formation with Mild Plasma Treatment. *ACS Nano* **2016**, *10*, 6853–6860.

(27) Blades, W. H.; Frady, N. J.; Litwin, P. M.; McDonnell, S. J.; Reinke, P. Thermally Induced Defects on WSe_2. *J. Phys. Chem. C* **2020**, *124*, 15337–15346.

(28) Simon, D. K.; Jordan, P. M.; Mikolajick, T.; Dirnstorfer, I. On the Control of the Fixed Charge Densities in Al_2O_3-Based Silicon Surface Passivation Schemes. *ACS Appl. Mater. Interfaces* **2015**, *7*, 28215–28222.

(29) Graham, R.; Miller, C.; Oh, E.; Yu, D. Electric Field Dependent Photocurrent Decay Length in Single Lead Sulfide Nanowire Field Effect Transistors. *Nano Lett.* **2011**, *11*, 717–722.

(30) Xiao, R.; Hou, Y.; Fu, Y.; Peng, X.; Wang, Q.; Gonzalez, E.; Jin, S.; Yu, D. Photocurrent Mapping in Single-Crystal Methylammonium Lead Iodide Perovskite Nanostructures. *Nano Lett.* **2016**, *16*, 7710–7717.

(31) Cui, Q.; Ceballos, F.; Kumar, N.; Zhao, H. Transient Absorption Microscopy of Monolayer and Bulk WSe_2. *ACS Nano* **2014**, *8*, 2970–2976.

(32) Chen, X.; Wang, Z.; Wang, L.; Wang, H. Y.; Yue, Y. Y.; Wang, H.; Wang, X. P.; Wee, A. T. S.; Qiu, C. W.; Sun, H. B. Investigating the Dynamics of Excitons in Monolayer WSe_2 Before and After Organic Super Acid Treatment. *Nanoscale* **2018**, *10*, 9346–9352.

(33) Movva, H. C. P.; Rai, A.; Kang, S.; Kim, K.; Fallahazad, B.; Taniguchi, T.; Watanabe, K.; Tutuc, E.; Banerjee, S. K. High-Mobility Holes in Dual-Gated WSe_2 Field-Effect Transistors. *ACS Nano* **2015**, *9*, 10402–10410.

(34) Miller, E. J.; Yu, E. T.; Waltereit, P.; Speck, J. S. Analysis of Reverse-Bias Leakage Current Mechanisms in GaN Grown by Molecular-Beam Epitaxy. *Appl. Phys. Lett.* **2004**, *84*, 535–537.

(35) Wittmer, M. Conduction Mechanism in PtSi/Si Schottky Diodes. *Phys. Rev. B: Condens. Matter* **1991**, *43*, 4385–4395.

(36) Werner, J. H.; Güttler, H. H. Transport Properties of Inhomogeneous Schottky Contacts. *Phys. Scr.* **1991**, *T39*, 258–264.

(37) Laurent, M. A.; Gupta, G.; Suntrup, D. J., III; DenBaars, S. P.; Mishra, U. K. Barrier Height Inhomogeneity and its Impact on (Al,In,Ga)N Schottky Diodes. *J. Appl. Phys.* **2016**, *119*, No. 064501.

(38) Lee, J. I.; Brini, J.; Dimitriadis, C. A. Simple Parameter Extraction Method for Non-Ideal Schottky Barrier Diodes. *Electron. Lett.* **1998**, *34*, 1268–1269.

(39) Nourbakhsh, A.; Zubair, A.; Dresselhaus, M. S.; Palacios, T. Transport Properties of a MoS_2/WSe_2 Heterojunction Transistor and Its Potential for Application. *Nano Lett.* **2016**, *16*, 1359–1366.

(40) Zhu, Y.; Zhou, R.; Zhang, F.; Appenzeller, J. Vertical Charge Transport Through Transition Metal Dichalcogenides - A Quantitative Analysis. *Nanoscale* **2017**, *9*, 19108–19113.

(41) Zubair, A.; Nourbakhsh, A.; Hong, J.-Y.; Qi, M.; Song, Y.; Jena, D.; Kong, J.; Dresselhaus, M.; Palacios, T. Hot Electron Transistor with van der Waals Base-Collector Heterojunction and High-Performance GaN Emitter. *Nano Lett.* **2017**, *17*, 3089–3096.